The Influence of Ground-Relative Flow and Friction on Near-Surface Storm-Relative Helicity

MATTHEW D. FLOURNOY[a] AND ERIK N. RASMUSSEN[a]

[a] *Cooperative Institute for Mesoscale Meteorological Studies, NOAA/OAR National Severe Storms Laboratory, Norman, Oklahoma*

(Manuscript received 19 October 2020, in final form 20 April 2021)

ABSTRACT: Recent studies have highlighted the importance of near-ground storm-relative helicity (SRH) in supercell and tornado processes and how surface friction can play a role. In this study, we use an analytical approach to examine how uniform changes to the ground-relative wind profile above the near-ground layer influence SRH within the near-ground layer. We show how the ground-relative influence of surface friction alters the near-ground shear profile. For idealized semicircular and straight shear profiles, increasing preexisting ground-relative flow above the near-ground layer yields increasing SRH. The magnitude of the SRH increase is sensitive to storm motion, with more deviant motion yielding greater SRH increases given the same increase in ground-relative flow. Supercells may be more susceptible to storm-induced SRH enhancements given their deviant motion and ability to increase ground-relative flow in the background environment.

KEYWORDS: Wind shear; Storm environments; Friction

1. Introduction and motivation

The amount of streamwise horizontal vorticity in the background environment is critical in determining the potential for a thunderstorm to develop into a supercell. The midlevel mesocyclone, the defining characteristic of a supercell, forms via tilting of ambient streamwise vorticity (Davies-Jones 1984; Dahl 2017). The low-level mesocyclone forms in a similar manner (e.g., Markowski and Richardson 2014) with baroclinity also playing a role (e.g., Rotunno and Klemp 1985; Dahl et al. 2014). To this end, the amount of streamwise horizontal vorticity is incorporated into forecasting parameters to help predict supercell potential and strength. Storm-relative helicity (SRH) in the 0–1-km, 0–3-km, or effective layer is often used, which is a measure of both horizontal vorticity and storm-relative flow (e.g., Davies-Jones et al. 1990; Rasmussen and Blanchard 1998; Thompson et al. 2003; Craven and Brooks 2004). Given equal storm-relative flow, larger SRH implies larger streamwise vorticity and a stronger supercell.

The amount of streamwise horizontal vorticity, particularly at low levels, is also critical in determining the potential for a supercell to produce a tornado (e.g., Rasmussen 2003). Increased low-level SRH supports a stronger low-level mesocyclone via more efficient tilting (Markowski and Richardson 2014; Coffer and Parker 2017). This results in greater low-level upward dynamic accelerations and vertical vorticity stretching that, all else being equal, increases tornado potential. Recent studies also show that increased near-surface streamwise vorticity may play a more direct role in the tornado vorticity budget by being abruptly tilted and stretched upward into the vortex (Rotunno et al. 2017; Boyer and Dahl 2020). The critical angle, defined as the angle between the 10 m AGL storm-relative wind vector and the 10–500-m shear vector, helps diagnose the degree to which environmental vorticity is streamwise close to the surface (Esterheld and Giuliano 2008). A recent study also showed that using 0–500-m SRH instead of 0–1-km SRH in the calculation of the significant tornado parameter (Thompson et al. 2003) yields increased skill in discriminating between tornadic and nontornadic environments (Coffer et al. 2019).

As focus shifts to the vertical wind profile closer to the ground, the possible influences of friction become important. On the tornado scale, friction is important in disrupting cyclostrophic balance to promote inward radial acceleration and abrupt upward turning in the corner region (e.g., Fiedler and Rotunno 1986; Lewellen and Lewellen 2007). On the storm scale, recent studies show that surface friction can modify preexisting vorticity as well as generate horizontal vorticity that then plays a role in the vorticity budget of the tornado or low-level mesocyclone (Schenkman et al. 2014; Roberts et al. 2016; Markowski 2016; Mashiko 2016; Roberts and Xue 2017). A couple studies have also shown that surface friction influences tornado potential in quasi-linear convective systems (Schenkman et al. 2012; Xu et al. 2015). However, the relative importance of friction on the tornado budget in large-eddy simulations like these may be significantly overestimated due to an unrealistic lack of turbulence in the prestorm boundary layer (Markowski and Bryan 2016); as such, these studies probably represent the maximum extent to which friction modifies storm-scale and tornado vorticity budgets.

These studies motivate this initial work to examine the influence of surface friction on the storm-relative wind profile. In particular, we focus on the lowest hundreds of meters AGL where the relative amount of streamwise and crosswise vorticity may more strongly influence supercell and tornado potential (e.g., Thompson and Edwards 2000; Esterheld and Giuliano 2008; Coffer and Parker 2017; Guarriello et al. 2018). We were inspired by the methods of Markowski (2016) who created their DRAG-CROSSWISE and DRAG-STREAMWISE cases

Corresponding author: Matthew Flournoy, matthew.flournoy@noaa.gov

DOI: 10.1175/JAS-D-20-0320.1

simply by shifting the semicircular, ground-relative wind profile away from the origin [see Markowski's (2016) Fig. 2]. Assuming a storm motion at the center of the semicircular portion of the hodograph (to be discussed later), the profile with faster ground-relative winds yielded increased streamwise vorticity and storm-relative flow in the near-surface layer influenced by friction. Both of these characteristics contributed to larger near-surface SRH in the DRAG-STREAMWISE experiment. Further examining the influence of increased ground-relative flow on near-surface SRH due to friction may help explain how some storms modify their background environment (e.g., Parker 2014; Wade et al. 2018; Coniglio and Parker 2020).

The influence of the wind profile on supercell morphology is often described as Galilean invariant because storm-internal processes depend on vertical wind shear rather than just the wind (e.g., Bunkers et al. 2000). However, friction is *ground*-relative, violating Galilean invariance, and will always result in a near-surface wind profile extending to the origin, regardless of where the rest of the wind profile lurks in hodograph space. This yields the following question: how do ground-relative winds and friction influence near-ground SRH?

2. Creating the frictionally induced shear profile

We use a simple analytical approach to address the question of how surface friction influences the storm-relative wind profile. First, a base-state wind profile is constructed using the semicircular hodograph originally presented in McCaul and Weisman (2001) and also used by Markowski (2016). In this framework, the wind components are specified as

$$\overline{v}(z) = \frac{Amz}{H}\exp\left(1-\frac{mz}{H}\right) + \Delta y, \tag{1}$$

$$\overline{u}(z) = \mathrm{sgn}(z - z_0)(A^2 + \overline{v}^2)^{1/2} + \Delta x, \tag{2}$$

where $\overline{u}$ and $\overline{v}$ are the zonal and meridional wind components, z is the vertical coordinate, A is the hodograph radius, m is the profile "compression parameter," H is the vertical scale, z_0 is the height where $\overline{v}(z)$ is a maximum, and Δx and Δy are zonal and meridional differences introduced in this study that shift the center of the hodograph. Absent friction, Δx and Δy would not alter SRH because of Galilean invariance. The compression parameter alters the layers in which the largest shear is concentrated, with larger values of m corresponding to profiles with larger shear in low levels [see Fig. 1 of Markowski and Richardson (2014) for an example]. The hodographs here use the same parameters as the "strong-shear" simulation of Markowski and Richardson (2014): $A = 8\,\mathrm{m\,s^{-1}}$, $m = 8$, $H = 6\,\mathrm{km}$, and $z_0 = 750\,\mathrm{m}$. The resulting half-circle hodograph is shown in black in Fig. 1 ($\Delta x = \Delta y = 0$). This hodograph shape is used for convenience in relating our work to previous studies and identifying the resulting updraft motion, which is close to the center of the half-circle (e.g., Markowski and Richardson 2014; Markowski 2016). (We examine the impact of this assumption later in section 3c.) The black hodograph shown in Fig. 1 has nonzero velocity at 0 m AGL and thus does not include the effects of surface friction.

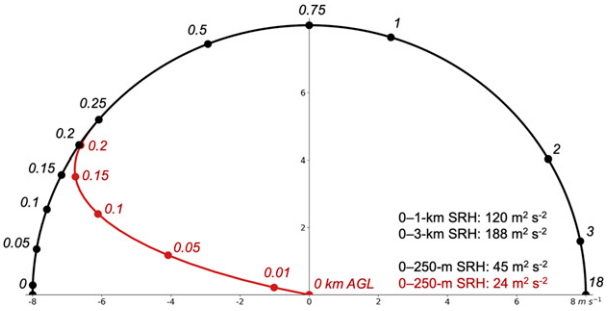

FIG. 1. The semicircle hodographs used in this study with no near-surface frictional effects (black) and near-surface frictional effects included below 250 m AGL (red). The black hodograph is identical to the strong-shear simulation ($m = 8$) of Markowski and Richardson (2014, their Fig. 1b). The profiles are plotted in ground-relative, u–v space ($\mathrm{m\,s^{-1}}$) and heights of interested are indicated (km). The 0–1- and 0–3-km SRH values are shown for the half-circle profile as well as 0–250-m SRH for each profile. Different storm motions are used for calculating SRH, including motion at the center of the half-circle (i.e., at the origin for the case plotted here) and Bunkers-right storm motion.

Next, we include a simple parameterization to represent the effect of surface friction on the near-ground wind profile to bring the surface wind to zero. Various methods to accomplish a steady-state, near-ground hodograph in the presence of surface friction in numerical models exist. These include applying "force-restore" terms to approximate the effects of large-scale Coriolis and pressure-gradient forces (Markowski 2016), applying geotriptic balance between the frictional, Coriolis, and pseudopressure-gradient force forces to arrive at a slightly modified, balance wind profile (Roberts et al. 2016), and applying a pseudopressure-gradient force to offset friction (Wilhelmson and Chen 1982; Dawson et al. 2019). However, this study does not involve numerical integration and the effects of pressure gradient, Coriolis, or frictional forces in time. As such, we use the following analytical method to calculate the wind components in the near-ground (ng) layer influenced by surface friction:

$$\overline{u}_{\mathrm{ng}}(z) = wu_l + (1-w)\overline{u}(z), \tag{3}$$

$$\overline{v}_{\mathrm{ng}}(z) = wv_l + (1-w)\overline{v}(z), \tag{4}$$

where u_l and v_l are the zonal and meridional components assuming a linear wind profile in the near-ground layer and w is the weight ($0 \le w \le 1$) of those linear components. The linear components are defined as

$$u_l = \frac{z}{z_f}\overline{u}(z = z_f), \tag{5}$$

$$v_l = \frac{z}{z_f}\overline{v}(z = z_f), \tag{6}$$

where z_f is the depth of the near-ground layer influenced by surface friction. Finally, the weight function is defined as

$$w = \left(1-\frac{z}{z_f}\right)\left[\frac{\exp\left(\frac{z_f - z}{z_f}\right) - 1}{e-1}\right]. \tag{7}$$

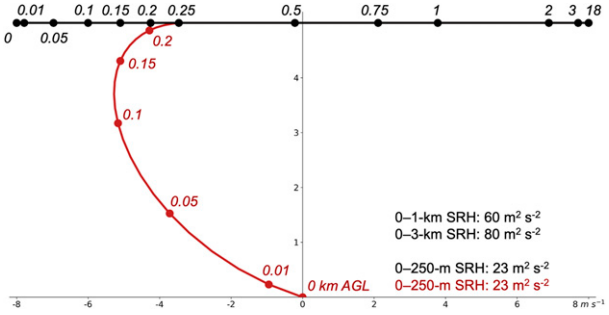

FIG. 2. As in Fig. 1, but for the straight hodograph case for $\Delta y = 5\,\mathrm{m\,s^{-1}}$ for the profiles with (red) and without (black) friction.

In general, this simple method assumes that the wind components in the near-ground layer influenced by friction are a function of the half-circle hodograph as well as a linear hodograph drawn from $z = 0$ to $z = z_f$. The influence of the linear component increases closer to the ground, mimicking the influence of surface friction. The result from applying this to the hodograph described above with $z_f = 250\,\mathrm{m}$ is shown in red in Fig. 1.[1] It is identical to the original hodograph except in the near-ground layer (defined by z_f) where it curves back to the origin at 0 m AGL. There are certainly other methods to derive a frictionally induced shear profile, which we briefly discuss in section 4. In particular, this profile ($\Delta x = \Delta y = 0$) is quite similar to the DRAG-CROSSWISE case of Markowski (2016; see their Fig. 2b) obtained after 2 h of integrating the semicircular hodograph in the presence of surface friction and force-restore terms that mimicked large-scale pressure gradient and Coriolis forces. Vorticity is largely crosswise in the near-ground layer (assuming a storm motion at the origin) but positive 0–250-m SRH exists ($24\,\mathrm{m^2\,s^{-2}}$).

To explore the role of friction on SRH with another commonly discussed hodograph, we apply a similar approach to construct straight hodographs with and without near-ground frictional effects. The base-state straight hodograph without frictional effects is computed as follows:

$$\overline{v}(z) = \Delta y, \tag{8}$$

$$\overline{u}(z) = A\left\{\frac{1}{e}\left[e - \exp\left(1 - \frac{mz}{H}\right)\right] - \frac{1}{2}\right\} + \Delta x. \tag{9}$$

The variables are the same as in Eq. (1) except that A in this case represents the length of the hodograph. Figure 2 shows the resulting hodograph in black for $\Delta y = 5\,\mathrm{m\,s^{-1}}$, $A = 16\,\mathrm{m\,s^{-1}}$, $H = 6000\,\mathrm{m}$, and $m = 8$. This influence of near-ground friction is not present in this hodograph (i.e., nonzero velocity at $z = 0\,\mathrm{m}$). To include friction, the near-ground profile is constructed in the same way as the semicircular case with the near-ground wind profile influenced by a linear and semicircular component. The linear components are calculated using Eqs. (5) and (6) and the semicircular components are calculated using Eqs. (1) and (2) from $z = 0$ to $z = z_f$ with $A = \Delta y$, $H = 6000\,\mathrm{m}$, $m = 24$, and $z_0 = z_f$. The resulting hodograph where $z_f = 250\,\mathrm{m}$ is shown in Fig. 2 (red line).

[1] The choice of 250 m is consistent with the average height of a hodograph kink found in Coniglio and Parker (2020). We discuss the impact of varying z_f later.

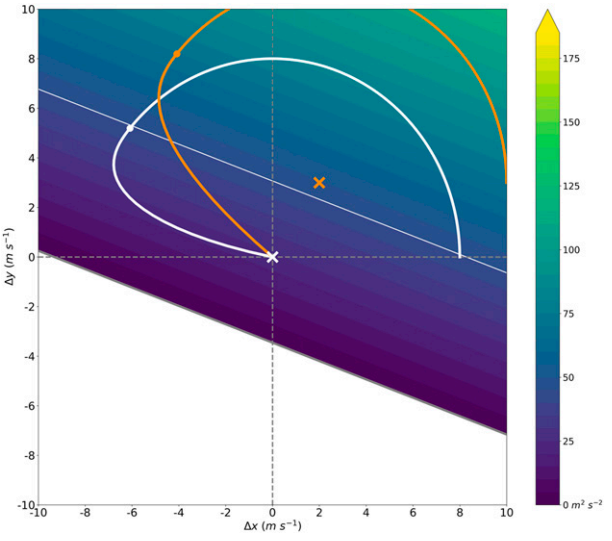

FIG. 3. The 0–250-m SRH (shading) calculated using the semicircular hodograph with near-surface frictional effects included at each $(\Delta x, \Delta y)$ point. The profiles at $\Delta x = \Delta y = 0$ and $(\Delta x, \Delta y) = (2, 3)$ are shown as examples (solid white and orange lines, respectively). $z_f = 250\,\mathrm{m}$ for these cases highlighted (white and orange dots), and the assumed storm motion at $(\Delta x, \Delta y)$ is shown (white and orange ×). Only positive SRH values are contoured. The thin white line is the value of 0–250-m SRH for the full half-circle profile without any frictional effects at the surface, roughly $45\,\mathrm{m^2\,s^{-2}}$ (constant for all Δx and Δy). The color bar shown here was chosen to match the color bar in Fig. 7 for ease of comparison.

3. Varying the ground-relative winds

a. Semicircular shear profile

To assess the combined influence of uniform changes of ground-relative flow and friction on near-surface horizontal vorticity orientation, Δx and Δy are varied. This results in a semicircular hodograph centered at $(\Delta x, \Delta y)$ with the same shear profile *above* z_f as the case in Fig. 1 where $\Delta x = \Delta y = 0$. The shear profile *below* z_f differs because of the bottom boundary condition, $\overline{u}(z) = \overline{v}(z) = 0$. This results in different magnitudes of horizontal vorticity, storm-relative flow, and SRH for each instance of Δx and Δy. The formulation of SRH is given as

$$\mathrm{SRH} = \int_{z_b}^{z_t} \boldsymbol{\omega}_h \cdot \mathbf{u}_{\mathrm{sr}}\, dz, \tag{10}$$

where $\boldsymbol{\omega}_h$ is the horizontal vorticity vector, $\mathbf{u}_{\mathrm{sr}}$ is the storm-relative horizontal wind vector, and z_b and z_t are the bottom and top of the layer of interest, respectively. Figure 3 shows the resulting 0–250-m SRH field for $z_f = 250\,\mathrm{m}$ as Δx and Δy vary from -10 to $10\,\mathrm{m\,s^{-1}}$. For now, we assume storm motion is at

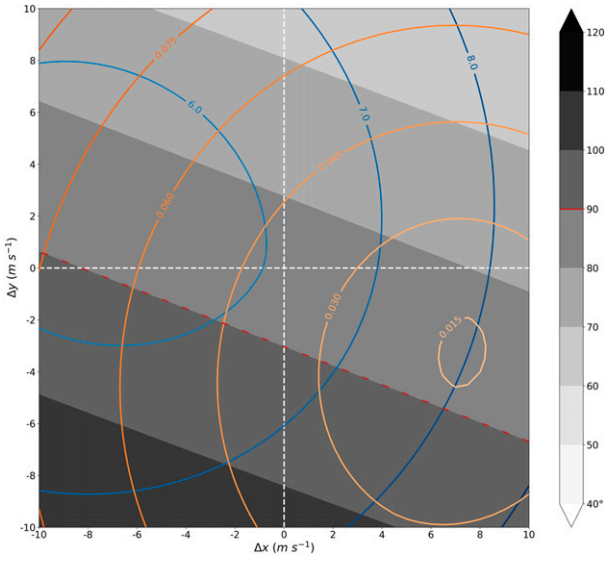

FIG. 4. Mean storm-relative wind speed (blue, m s^{-1}), horizontal vorticity magnitude (orange, s^{-1}), and the angle between the two (shading, in degrees) in the 0–250 m AGL layer for the half-circle profile with frictional effects (i.e., the same profile used in Fig. 3). The 90° isopleth is highlighted in red, which by definition lies along the 0 $m^2 s^{-2}$ isopleth plotted in Fig. 3.

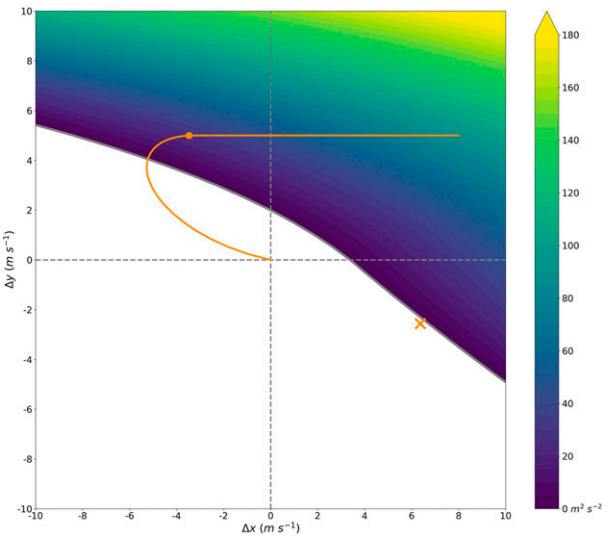

FIG. 5. As in Fig. 3, but for the straight profile with frictional effects included (see Fig. 2). The profile at $(\Delta x, \Delta y) = (0, 5)$ is shown as an example (orange line). The orange dot indicates the wind vector at 250 m AGL (z_f) and the orange × indicates the Bunkers-right storm motion used to calculate SRH for this profile (roughly 58 $m^2 s^{-2}$).

the center of the half-circle. Roughly 24 $m^2 s^{-2}$ of 0–250-m SRH exist when $\Delta x = \Delta y = 0$ (i.e., for the white hodograph plotted in Fig. 3). The 0–250-m SRH increases as Δx and Δy increase, or, more specifically, as ground-relative winds increase perpendicular and to the right of the frictionally induced shear vector. The orange profile in Fig. 3 for $(\Delta x, \Delta y) = (2, 3)$ provides an example of this with 0–250-m SRH near 50 $m^2 s^{-2}$. Given an expected storm motion at the center of the semicircle, moving the hodograph in this direction yields larger storm-relative wind magnitudes, larger horizontal vorticity magnitudes, and greater alignment between the two from 0 to 250 m AGL. To reiterate, SRH would be the same for both of the example hodographs absent the modification representing friction.

As defined in Eq. (10), SRH is a function of the magnitudes of $\boldsymbol{\omega}_h$ and $\mathbf{u}_{sr}$ as well as the angle between them. To further quantify the relative influences of these on SRH, we calculated the means of these variables in the 0–250 m AGL layer for all Δx and Δy. The result for the half-circle profile with frictional effects included (i.e., the profile used in Fig. 3) is shown in Fig. 4. By definition, the gradient of the angle between $\boldsymbol{\omega}_h$ and $\mathbf{u}_{sr}$ (Fig. 4) points in the opposite direction as the gradient of SRH (Fig. 3), and SRH = 0 $m^2 s^{-2}$ when the angle = 90°. As the angle decreases toward 0°, the projection of $\boldsymbol{\omega}_h$ onto $\mathbf{u}_{sr}$ increases, resulting in an increase in positive SRH. A minimum in $\boldsymbol{\omega}_h$ exists near $(\Delta x, \Delta y) = (7, -3)$ because in that case the ground-relative wind at 250 m lies at the origin, resulting in near-zero vertical wind shear from 0 to 250 m AGL. As the angle decreases (e.g., as Δx and Δy generally increase), $\boldsymbol{\omega}_h$ and $\mathbf{u}_{sr}$ increase. These influences all lead to increasing SRH (see Fig. 3). As the angle increases (e.g., as Δx and Δy generally decrease), $\boldsymbol{\omega}_h$ and $\mathbf{u}_{sr}$ increase, leading to negative SRH. As $\boldsymbol{\omega}_h$ and $\mathbf{u}_{sr}$ change but the angle remains constant (i.e., moving parallel to the shaded contours in Fig. 4), SRH remains constant.

In this analytical framework, changes in SRH are only possible if the angle between $\boldsymbol{\omega}_h$ and $\mathbf{u}_{sr}$ changes. When the angle changes, the magnitudes of $\boldsymbol{\omega}_h$ and $\mathbf{u}_{sr}$ influence the magnitude of the resulting change in SRH. Uniformly increasing ground-relative wind speeds throughout the hodograph (e.g., increasing Δx and Δy) above z_f results in larger SRH in the surface–z_f layer. This finding complements the analyses of Coniglio and Parker (2020) in showing how enhancements to the storm-relative wind profile in different layers can lead to substantial increases in SRH, and in their case discrimination between tornadic and nontornadic wind profiles. In this case, this is solely due to the influence of surface friction altering the near-ground shear profile.

b. *Unidirectional shear profile*

Next, Δx and Δy are varied in a similar manner for the straight hodograph under the influence of near-ground friction. As before, this results in identical hodograph shapes above z_f for all combinations of Δx and Δy but different shapes below z_f. As in Fig. 3, SRH values across the domain are plotted in Fig. 5. Rather than assuming the storm motion lies at the center of the straight hodograph, we use a more relevant assumption of Bunkers-right storm motion (Bunkers et al. 2000). This method has caveats—particularly related to predicting the motion of high-precipitation supercells (Ramsay and Doswell 2005) or supercells within environments with any of the characteristics noted in Bunkers (2018)—but is used here due to its general applicability and wide use. In the example profile plotted in

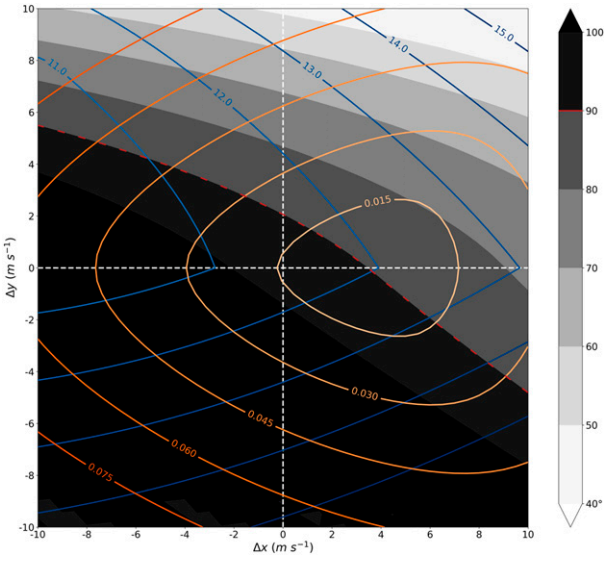

FIG. 6. As in Fig. 4, but for the straight profile with frictional effects included (i.e., the same profile used in Fig. 5).

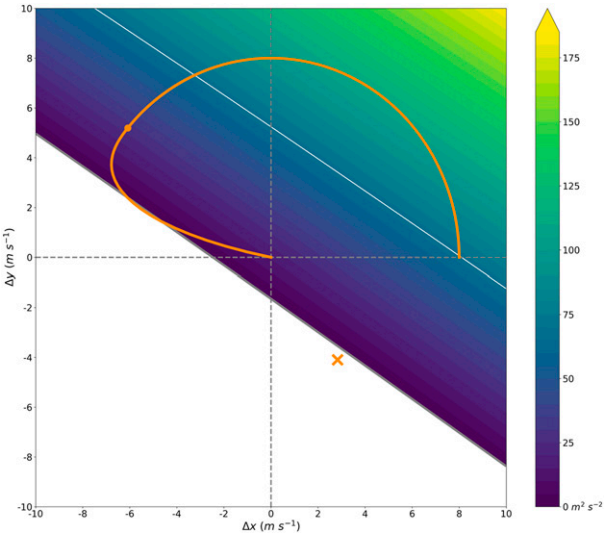

FIG. 7. As in Fig. 3, but assuming Bunkers-right storm motion. The profile at $\Delta x = \Delta y = 0$ is shown for reference. The white line is the value of 0–250-m SRH for the full half-circle profile without any frictional effects at the surface, roughly 67 $m^2 s^{-2}$ (constant for all Δx and Δy).

Fig. 5 at $(\Delta x, \Delta y) = (0, 5)$, roughly 58 $m^2 s^{-2}$ of 0–250-m SRH exists. At $(\Delta x, \Delta y) = (0, 0)$, the profile exists solely on the x axis and contains negative SRH due to the assumed Bunkers-right storm motion. Increasing Δx and Δy eventually overcomes this effect and yields positive 0–250-m SRH.

Much of the discussion above regarding the relative influences of $\boldsymbol{\omega}_h$, $\mathbf{u}_{sr}$, and the angle between the two on SRH for the half-circle profile also applies to the straight one (Fig. 6). The gradient of SRH (Fig. 5) points opposite the gradient of the angle between $\boldsymbol{\omega}_h$ and $\mathbf{u}_{sr}$. $\boldsymbol{\omega}_h$ is symmetric about the x axis due to the profile containing unidirectional westerly shear. $\mathbf{u}_{sr}$ is not symmetric about the x axis due to the Bunkers-right storm motion assumption. The direction of the SRH gradient is driven by the angle between $\boldsymbol{\omega}_h$ and $\mathbf{u}_{sr}$ and the magnitude of the SRH gradient is driven by the magnitudes of $\boldsymbol{\omega}_h$ and $\mathbf{u}_{sr}$. Within the same domain of Δx and Δy, a larger range of angles between $\boldsymbol{\omega}_h$ and $\mathbf{u}_{sr}$ exists for the straight profile than the half-circle one. The next subsection addresses whether this is due to the different shear profile or storm motion assumption.

c. Sensitivity to storm motion

Given identical ground-relative wind profiles, different storm motions yield different values of SRH. Are the changes to near-ground SRH induced by friction sensitive to the assumed storm motion? Fig. 7 shows the variation in 0–250-m SRH for the half-circle profile with frictional effects included (i.e., the same profile used in Fig. 3) but with storm motion following the Bunkers-right assumption rather than lying at the center of the half-circle. The results are indeed sensitive to storm motion. Within the same range of Δx and Δy, the range of positive 0–250-m SRH increases roughly 50% when Bunkers-right storm motion is used (cf. Figs. 3 and 7). The example profile at $\Delta x = \Delta y = 0$ contains less SRH than the case in Fig. 3 due to the presence of antistreamwise vorticity. However, as Δx and Δy increase, Bunkers-right motion continues to lie well to the right of the center of the half-circle, yielding larger SRH. Also, unlike the assumed motion at the center of the half-circle, Bunkers-right motion is slightly influenced by the changing wind profile from 0 to 250 m AGL. Both of these characteristics yield a larger gradient in SRH within the same range of Δx and Δy than in the original case.

d. Sensitivity to the height of the friction layer

Although Coniglio and Parker (2020) found an average hodograph "kink" height near 250 m AGL, varying atmospheric conditions like nocturnal stabilization or increased boundary layer mixing will alter this height. To assess the sensitivity of our results to variations in the "kink" height (i.e., the height at which hodograph curvature begins), we reproduced our analyses with $z_f = 100$ m and $z_f = 500$ m. Intuitively, profiles that are influenced by surface friction through a deeper layer (e.g., $z_f = 500$ m) exhibit greater SRH reductions. Compared to 24 $m^2 s^{-2}$ 0–250-m SRH in the $z_f = 250$-m analysis, setting $z_f = 500$ m resulted in 11 $m^2 s^{-2}$ 0–250-m SRH. Conversely, reducing z_f to 100 m yielded an increase in 0–250-m SRH to 36 $m^2 s^{-2}$, closer to the value when surface friction is not included (45 $m^2 s^{-2}$). The range of 0–250-m SRH increases due to varying Δx and Δy were similar between the $z_f = 100$-, 250-, and 500-m analyses. However, the direction of the SRH gradient changed depending on the orientation of the frictionally induced near-ground shear profile. For example, for $\Delta x = \Delta y = 0$, reducing the near-ground layer to 100 m yielded large, primarily easterly shear in that layer. As a result, increases in SRH due to enhanced ground-relative flow are larger for increases in Δy than Δx. Conversely, weaker, primarily southeasterly shear is present when the near-ground layer is increased to 500 m, supporting the largest SRH increases for equal increases in Δx and Δy. Although the ideal

combination of Δx and Δy resulting in the largest SRH increases changes slightly based on the assumed storm motion, the gradient is largest close to 90° to the right of the frictionally induced shear vector.

4. Discussion

The inspiration for this study was the assumed Galilean-invariant relationship between updraft morphology and the vertical wind profile. Bunkers et al. (2000) described this in detail with respect to storm motion. Using idealized, straight hodographs from the surface to 6 km AGL, they showed that the resulting left and right storm motions always lie in the same hodograph-relative position regardless of where the hodograph exists in u–v space. This is valid given their assumption that the near-ground profile is not influenced by friction. In this study, we showed that accounting for the influence of surface friction results in Galilean-variant storm-relative parameters. This is consistent with the methodology of Markowski (2016), who simulated the effect of streamwise versus crosswise near-ground vorticity on ''pseudo-storm'' evolution by simply moving the ground-relative wind profile [Markowski's (2016) Fig. 2].

As discussed earlier, numerous methods exist to parameterize the influence of surface friction on the vertical wind profile in numerical simulations. These methods were not applied in this study due to its analytical nature. Rather, we parameterize the influence of surface friction using the same approach that we used to create the semicircular and straight hodographs but with the bottom boundary condition that $\overline{u}(z) = \overline{v}(z) = 0$. Using this approach allowed us to emulate the presence of surface friction without integrating force terms and yielded a realistic near-ground wind profile similar to those obtained after integration in past studies (e.g., Markowski 2016). Calculating the near-ground wind profile using a different approach will quantitively alter the impact of surface friction, but incorporating other formulations of the friction layer is beyond the scope of this paper. Because our approach yielded profiles similar to those from past studies, we believe our findings are generally applicable and would not qualitatively change if a different representation of surface friction were used.

These results may be relevant for better understanding the impact of storm-environment modifications on the local wind profile. Recent studies have shown that ground- and storm-relative winds strengthen in the vicinity of supercells (Parker 2014; Wade et al. 2018; Coniglio and Parker 2020). The physical processes responsible for this remain mostly unexplored but are probably related to the strength of the supercell updraft (meso-γ scale) and compensating inward horizontal accelerations (meso-β scale). Flournoy et al. (2020) showed that these enhancements to the wind profile can result in a local environment much more conducive for tornado production. The findings shown here represent one way in which these modifications can result in such an environment. In particular, uniformly increasing wind speeds above the near-ground layer—which has no *direct* impact on storm-relative parameters like SRH within the near-ground layer—was shown to *indirectly* (and substantially) increase near-ground SRH due to friction (i.e., the no-slip condition at the surface).

This is consistent with recent findings from Wade et al. (2018) and Coniglio and Parker (2020) related to the environments of tornadic supercells. In particular, Wade et al. (2018) found enhanced ground- and storm-relative winds in the near inflow of tornadic supercells but not nontornadic ones [Wade et al.'s (2018) Fig. 7b]. Much of this enhancement is attributable to a relatively uniform increase in the poleward, ground-relative wind component below 2 km AGL. Such a scenario is represented in our study by a positive Δy, yielding increased near-ground SRH even if storm motion also moves poleward. The cause for this enhancement near tornadic supercells rather than nontornadic supercells is likely the presence of a stronger mesocyclone in the tornadic cases (Coniglio and Parker 2020). Additionally, Coniglio and Parker (2020) found larger storm-relative winds and SRH, especially from 1 to 3 km AGL, near tornadic supercells than nontornadic ones due to both stronger ground-relative winds and more rightward-deviant storm motions. These findings are not entirely captured in this study because in our case, storm motion is ''latched'' to the wind profile. Conversely, Coniglio and Parker (2020) examine changes to the storm-relative wind profile due to changes in storm motion while holding the ground-relative wind profile steady [see Coniglio and Parker's (2020) Fig. 9]. These analyses are complementary in showing that enhancements to the poleward, ground-relative wind profile (i.e., increasing Δx and especially Δx) combined with increasingly rightward deviations yield increased SRH both in the near-ground layer and aloft. This is because enhanced poleward ground-relative flow permits the same ratio of streamwise vorticity for increasingly rightward deviations.

This is exemplified in Fig. 8 using a wind profile adapted from the composite tornadic profile obtained in Coniglio and Parker (2020, their Fig. 10a); the ''original'' profile and associated 0–250-m and 1–3-km SRH areas (computed using the Bunkers-right estimate shown) are shown in blue, and the ''original'' profile with $\Delta y = 5\,\mathrm{m\,s^{-1}}$ (e.g., the ''enhanced'' profile) is shown in orange. In this schematic, storm motion is ''latched'' to each wind profile above the near-ground layer such that 1–3-km SRH is identical in both cases. However, as we have shown analytically, the ''enhanced'' profile contains more SRH in the near-ground layer (shown here as the 0–250-m layer). Finally, if a storm deviated more to the right in the ''enhanced'' profile, it would encounter more 0–250-m SRH *and* more 1–3-km SRH above the near-ground layer than the ''original'' case, as shown by the red dashed lines (e.g., Coniglio and Parker 2020). This shows how the analytical framework presented here may be realized in observed supercells, along with increasingly rightward deviant motions, to yield increased SRH aloft and in the near-ground layer to support tornadic supercells.

5. Summary

This study addressed the following question: *how do ground-relative winds and surface friction influence near-ground SRH?* The motivation posing this question was to further analyze

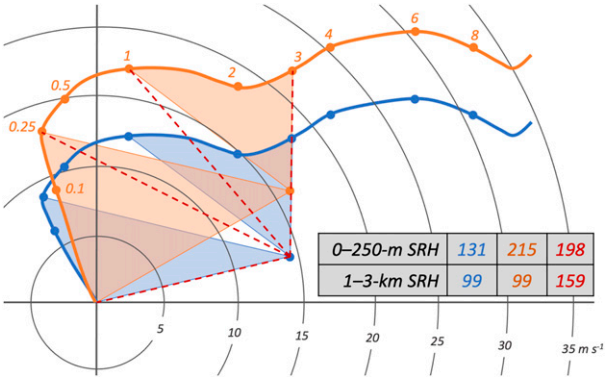

FIG. 8. Schematic showing the combined influences of increasing Δy and an increasingly rightward deviant storm motion in ground-relative hodograph space. The "original" profile (blue) is derived from the tornadic composite profile obtained in Coniglio and Parker (2020; their Fig. 10a). The "enhanced" profile (orange) is the "original" profile with $\Delta y = 5\,\mathrm{m\,s^{-1}}$ added above $z_f = 250\,\mathrm{m}$. Orange and blue shaded areas indicate 0–250-m and 1–3-km SRH areas for each profile. The orange and blue circles that lie off of the profiles show the Bunkers-right storm motion estimate for each profile from which SRH is computed. The red dashed lines indicate SRH computed for an increasingly rightward deviant storm in an environment characterized by the "enhanced" wind profile. Heights (km AGL) are shown (only orange labels are shown). The 0–250-m and 0–1-km SRH values ($\mathrm{m^2\,s^{-2}}$) are shown for the original (blue), enhanced (orange), and deviant (red) cases.

relationships between the vertical wind profile and updraft morphology, which are commonly assumed to be Galilean invariant. This assumption relies on the fact that storm morphology depends on the vertical shear profile and not the vertical wind profile. However, we hypothesized that the influence of surface friction, a ground-relative and Galilean variant presence, would meaningfully influence the shear profile.

We used an analytical approach to answer this question. Solutions for idealized semicircular and straight hodographs were drawn from the methods of McCaul and Weisman (2001), Markowski and Richardson (2014), and Markowski (2016). The wind profile influenced by surface friction within the near-ground layer (defined here as 0–250 m AGL) was derived from semicircular and linear components and resembled profiles presented in past numerical and observational studies. Uniform changes to the wind profile were introduced above the friction layer to examine the influence of ground-relative flow and friction on the near-ground, storm-relative wind profile.

We quantified the relationship between the vertical wind profile and near-ground SRH, which is not Galilean invariant when accounting for surface friction. This is because surface friction is a ground-relative process that ultimately influences the shear profile impacting updraft development. Previous studies have shown the importance of storm-relative characteristics in this layer in influencing storm morphology, especially with respect to tornado potential in supercells. For cases featuring idealized semicircular and straight wind profiles, increasing ground-relative wind speeds above the near-ground layer yielded increased SRH within the near-ground layer. The magnitude of the increase in SRH was sensitive to storm motion. This is representative of storm-induced modifications to the background wind profile and highlights one way that these processes may create a local environment more supportive of supercell and tornado potential without changing the shear profile above the friction layer. Furthermore, supercells may be more susceptible to storm-induced SRH enhancements due to their deviant motion.

Should storms evolve differently in different shear and friction regimes even if storm-relative parameters like effective bulk shear, winds, and helicity are equal? And, of course, what is the best way to parameterize surface friction in numerical models? Observations of the boundary layer, like those obtained by lidar and unmanned aerial platforms, will continue to help characterize the near-ground profile. These should better inform the methods of numerical studies in parameterizing the near-ground friction layer and its subsequent influence on storm morphology.

Acknowledgments. We thank Michael Coniglio and three anonymous reviewers for their insightful comments that improved this paper. Funding was provided by NOAA/Office of Oceanic and Atmospheric Research under NOAA–University of Oklahoma Cooperative Agreement NA11OAR4320072, U.S. Department of Commerce. The statements, findings, conclusions, and recommendations are those of the authors and do not necessarily reflect the views of NOAA or the U.S. Department of Commerce.

Data availability statement. The code used for the analysis presented in this paper is available online in a GitHub repository at mdflournoy/friction-srh.

REFERENCES

Boyer, C. H., and J. M. L. Dahl, 2020: The mechanisms responsible for large near-surface vertical vorticity within simulated supercells and quasi-linear storms. *Mon. Wea. Rev.*, **148**, 4281–4297, https://doi.org/10.1175/MWR-D-20-0082.1.

Bunkers, M. J., 2018: Observations of right-moving supercell motion forecast errors. *Wea. Forecasting*, **33**, 145–159, https://doi.org/10.1175/WAF-D-17-0133.1.

——, B. A. Klimowski, J. W. Zeitler, R. L. Thompson, and M. L. Weisman, 2000: Predicting supercell motion using a new hodograph technique. *Wea. Forecasting*, **15**, 61–79, https://doi.org/10.1175/1520-0434(2000)015<0061:PSMUAN>2.0.CO;2.

Coffer, B. E., and M. D. Parker, 2017: Simulated supercells in nontornadic and tornadic VORTEX2 environments. *Mon. Wea. Rev.*, **145**, 149–180, https://doi.org/10.1175/MWR-D-16-0226.1.

——, ——, R. L. Thompson, B. T. Smith, and R. E. Jewell, 2019: Using near-ground storm relative helicity in supercell tornado forecasting. *Wea. Forecasting*, **34**, 1417–1435, https://doi.org/10.1175/WAF-D-19-0115.1.

Coniglio, M. C., and M. D. Parker, 2020: Insights into supercells and their environments from three decades of targeted radiosonde observations. *Mon. Wea. Rev.*, **148**, 4893–4915, https://doi.org/10.1175/MWR-D-20-0105.1.

Craven, J. P., and H. E. Brooks, 2004: Baseline climatology of sounding derived parameters associated with deep, moist convection. *Natl. Wea. Dig.*, **28**, 13–24.

Dahl, J. M. L., 2017: Tilting of horizontal shear vorticity and the development of updraft rotation in supercell thunderstorms. *J. Atmos. Sci.*, **74**, 2997–3020, https://doi.org/10.1175/JAS-D-17-0091.1.

——, M. D. Parker, and L. J. Wicker, 2014: Imported and storm-generated near-ground vertical vorticity in a simulated supercell. *J. Atmos. Sci.*, **71**, 3027–3051, https://doi.org/10.1175/JAS-D-13-0123.1.

Davies-Jones, R., 1984: Streamwise vorticity: The origin of updraft rotation in supercell storms. *J. Atmos. Sci.*, **41**, 2991–3006, https://doi.org/10.1175/1520-0469(1984)041<2991:SVTOOU>2.0.CO;2.

——, D. W. Burgess, and M. Foster, 1990: Test of helicity as a tornado forecast parameter. *16th Conf. on Severe Local Storms*, Kananaskis Park, AB, Canada, Amer. Meteor. Soc., 588–592.

Dawson, D. T., II, B. Roberts, and M. Xue, 2019: A method to control the environmental wind profile in idealized simulations of deep convection with surface friction. *Mon. Wea. Rev.*, **147**, 3935–3954, https://doi.org/10.1175/MWR-D-18-0462.1.

Esterheld, J. M., and D. J. Giuliano, 2008: Discriminating between tornadic and non-tornadic supercells: A new hodograph technique. *Electron. J. Severe Storms Meteor.*, **3** (2), https://ejssm.org/ojs/index.php/ejssm/article/view/33/37.

Fiedler, B. H., and R. Rotunno, 1986: A theory for the maximum windspeeds in tornado-like vortices. *J. Atmos. Sci.*, **43**, 2328–2340, https://doi.org/10.1175/1520-0469(1986)043<2328:ATOTMW>2.0.CO;2.

Flournoy, M. D., M. C. Coniglio, E. N. Rasmussen, J. C. Furtado, and B. E. Coffer, 2020: Modes of storm-scale variability and tornado potential in VORTEX2 near- and far-field tornadic environments. *Mon. Wea. Rev.*, **148**, 4185–4207, https://doi.org/10.1175/MWR-D-20-0147.1.

Guarriello, F., C. J. Nowotarski, and C. C. Epifanio, 2018: Effects of the low-level wind profile on outflow position and near-surface vertical vorticity in simulated supercell thunderstorms. *J. Atmos. Sci.*, **75**, 731–753, https://doi.org/10.1175/JAS-D-17-0174.1.

Lewellen, D. C., and W. S. Lewellen, 2007: Near-surface intensification of tornado vortices. *J. Atmos. Sci.*, **64**, 2176–2194, https://doi.org/10.1175/JAS3965.1.

Markowski, P. M., 2016: An idealized numerical simulation investigation of the effects of surface drag on the development of near-surface vertical vorticity in supercell thunderstorms. *J. Atmos. Sci.*, **73**, 4349–4385, https://doi.org/10.1175/JAS-D-16-0150.1.

——, and Y. P. Richardson, 2014: The influence of environmental low-level shear and cold pools on tornadogenesis: Insights from idealized simulations. *J. Atmos. Sci.*, **71**, 243–275, https://doi.org/10.1175/JAS-D-13-0159.1.

——, and G. H. Bryan, 2016: LES of laminar flow in the PBL: A potential problem for convective storm simulations. *Mon. Wea. Rev.*, **144**, 1841–1850, https://doi.org/10.1175/MWR-D-15-0439.1.

Mashiko, W., 2016: A numerical study of the 6 May 2012 Tsukuba City supercell tornado. Part II: Mechanisms of tornadogenesis. *Mon. Wea. Rev.*, **144**, 3077–3098, https://doi.org/10.1175/MWR-D-15-0122.1.

McCaul, E. W., and M. L. Weisman, 2001: The sensitivity of simulated supercell structure and intensity to variations in the shapes of environmental buoyancy and shear profiles. *Mon. Wea. Rev.*, **129**, 664–687, https://doi.org/10.1175/1520-0493(2001)129<0664:TSOSSS>2.0.CO;2.

Parker, M. D., 2014: Composite VORTEX2 supercell environments from near-storm soundings. *Mon. Wea. Rev.*, **142**, 508–529, https://doi.org/10.1175/MWR-D-13-00167.1.

Ramsay, H. A., and C. A. Doswell, 2005: A sensitivity study of hodograph-based methods for estimating supercell motion. *Wea. Forecasting*, **20**, 954–970, https://doi.org/10.1175/WAF889.1.

Rasmussen, E. N., 2003: Refined supercell and tornado forecast parameters. *Wea. Forecasting*, **18**, 530–535, https://doi.org/10.1175/1520-0434(2003)18<530:RSATFP>2.0.CO;2.

——, and D. O. Blanchard, 1998: A baseline climatology of sounding-derived supercell and tornado forecast parameters. *Wea. Forecasting*, **13**, 1148–1164, https://doi.org/10.1175/1520-0434(1998)013<1148:ABCOSD>2.0.CO;2.

Roberts, B., and M. Xue, 2017: The role of surface drag in mesocyclone intensification leading to tornadogenesis within an idealized supercell simulation. *J. Atmos. Sci.*, **74**, 3055–3077, https://doi.org/10.1175/JAS-D-16-0364.1.

——, ——, A. D. Schenkman, and D. T. Dawson, 2016: The role of surface drag in tornadogenesis within an idealized supercell simulation. *J. Atmos. Sci.*, **73**, 3371–3395, https://doi.org/10.1175/JAS-D-15-0332.1.

Rotunno, R., and J. Klemp, 1985: On the rotation and propagation of simulated supercell thunderstorms. *J. Atmos. Sci.*, **42**, 271–292, https://doi.org/10.1175/1520-0469(1985)042<0271:OTRAPO>2.0.CO;2.

——, P. M. Markowski, and G. H. Bryan, 2017: "Near ground" vertical vorticity in supercell thunderstorm models. *J. Atmos. Sci.*, **74**, 1757–1766, https://doi.org/10.1175/JAS-D-16-0288.1.

Schenkman, A. D., M. Xue, and A. Shapiro, 2012: Tornadogenesis in a simulated mesovortex within a mesoscale convective system. *J. Atmos. Sci.*, **69**, 3372–3390, https://doi.org/10.1175/JAS-D-12-038.1.

——, ——, and M. Hu, 2014: Tornadogenesis in a high-resolution simulation of the 8 May 2003 Oklahoma City supercell. *J. Atmos. Sci.*, **71**, 130–154, https://doi.org/10.1175/JAS-D-13-073.1.

Thompson, R. L., and R. Edwards, 2000: An overview of environmental conditions and forecast implications of the 3 May 1999 tornado outbreak. *Wea. Forecasting*, **15**, 682–699, https://doi.org/10.1175/1520-0434(2000)015<0682:AOOECA>2.0.CO;2.

——, ——, J. A. Hart, K. L. Elmore, and P. Markowski, 2003: Close proximity soundings within supercell environments obtained from the Rapid Update Cycle. *Wea. Forecasting*, **18**, 1243–1261, https://doi.org/10.1175/1520-0434(2003)018<1243:CPSWSE>2.0.CO;2.

Wade, A. R., M. C. Coniglio, and C. L. Ziegler, 2018: Comparison of near- and far-field supercell inflow environments using radiosonde observations. *Mon. Wea. Rev.*, **146**, 2403–2415, https://doi.org/10.1175/MWR-D-17-0276.1.

Wilhelmson, R. B., and C.-S. Chen, 1982: A simulation of the development of successive cells along a cold outflow boundary. *J. Atmos. Sci.*, **39**, 1466–1483, https://doi.org/10.1175/1520-0469(1982)039<1466:ASOTDO>2.0.CO;2.

Xu, X., M. Xue, and Y. Wang, 2015: The genesis of mesovortices within a real-data simulation of a bow echo system. *J. Atmos. Sci.*, **72**, 1963–1986, https://doi.org/10.1175/JAS-D-14-0209.1.